

Revealing unusual bandgap shifts with temperature and bandgap renormalization effect in phase-stabilized metal halide perovskite thin films

Haochen Zhang^{1,2,#}, Zhixuan Bi^{1,#}, Zehua Zhai^{1,#}, Han Gao³, Yuwei Liu⁴, Meiling Jin⁴, Meng Ye⁵, Xuanzhang Li¹, Haowen Liu¹, Yuegang Zhang¹, Xiang Li⁴, Hairen Tan^{3,6,*}, Yong Xu^{1,7,8,*}, Luyi Yang^{1,2,7,8,*}

¹State Key Laboratory of Low Dimensional Quantum Physics, Department of Physics, Tsinghua University, Beijing 100084, China

²Department of Physics, University of Toronto, Toronto, Ontario M5S 1A7, Canada

³National Laboratory of Solid State Microstructures, Collaborative Innovation Center of Advanced Microstructures, Jiangsu Key Laboratory of Artificial Functional Materials, College of Engineering and Applied Sciences, Nanjing University, Nanjing 210093, China

⁴Center for Quantum Physics, School of Physics, Beijing Institute of Technology, Beijing 100081, China

⁵Graduate School of China Academy of Engineering Physics, Beijing 100193, China

⁶Frontiers Science Center for Critical Earth Material Cycling, Nanjing University, Nanjing 210093, China.

⁷Frontier Science Center for Quantum Information, Beijing 100084, China

⁸Collaborative Innovation Center of Quantum Matter, Beijing 100084, China

#These authors contributed equally.

*e-mail: hairentan@nju.edu.cn; yongxu@mail.tsinghua.edu.cn; luyi-yang@mail.tsinghua.edu.cn

Abstract

Hybrid organic-inorganic metal halide perovskites are emerging materials in photovoltaics, whose bandgap is one of the most crucial parameters governing their light harvesting performance. Here we present the temperature and photocarrier density dependence of the bandgap in two phase-stabilized perovskite thin films ($\text{MA}_{0.3}\text{FA}_{0.7}\text{PbI}_3$ and $\text{MA}_{0.3}\text{FA}_{0.7}\text{Pb}_{0.5}\text{Sn}_{0.5}\text{I}_3$) using photoluminescence and absorption spectroscopy. Contrasting bandgap shifts with temperature are observed between the two perovskites. Using X-ray diffraction and in situ high-pressure photoluminescence spectroscopy, we show that thermal expansion plays only a minor

role in the large bandgap blueshift, which is attributed to the enhanced structural stability of our samples. Our first-principles calculations further demonstrate the significant impact of thermally induced lattice distortions on the bandgap widening. We propose that the anomalous trends are caused by the competition between static and dynamic distortions. Additionally, both the bandgap renormalization and band filling effects are directly observed for the first time in fluence-dependent photoluminescence measurements and are employed to estimate the exciton effective mass. Our results provide new insights into the basic understanding of thermal and charge-accumulation effects on the band structure of hybrid perovskite thin films.

Keywords: phased-stabilized hybrid organic-inorganic perovskites, bandgap shift with temperature, lattice distortion, band filling effect, bandgap renormalization effect, photoluminescence, absorption spectroscopy

1. Introduction

Over the past few years, compositional engineering has made dramatic breakthroughs in improving the stability and efficiency of thin-film perovskite solar cells¹⁻³. Metal halide perovskites, with the formula ABX_3 (where A = Cs, methylammonium (MA), or formamidinium (FA); B = Pb or Sn; X = Cl, Br, or I), provide great opportunities to tune their bandgap and structural properties through alloying. While the inorganic octahedral framework $[BX_6]^{4-}$ directly determines the optoelectronic properties of perovskites, the characteristics of the A-site cation (size, motion, spatial distribution, etc.) play an important role in their structural stability by affecting the bond lengths and distortion angles of the inorganic lattice^{3,4}. Examples of alloying in perovskites include: (1) partially substituting FA^+ (ionic radius 2.53 Å) with the smaller-sized MA^+ (2.17 Å), which suppresses the undesired cubic-to-hexagonal transition and stabilizes the photoactive cubic phase at room temperature⁵; (2) partially replacing Pb with Sn reduces the bandgap so that more near-infrared light is absorbed². Both experimental and theoretical studies have pointed out that: (1) for double organic cation (MA_xFA_{1-x}) perovskites, the best thermodynamic stability is achieved at $x \approx 0.3$ (Refs.^{6,7}); (2) for mixed lead-tin (Pb_ySn_{1-y}) perovskites, $y \approx 0.5$ yields the smallest bandgap^{8,9}.

As light harvesters, one of the most crucial optoelectronic properties of perovskites is the optical bandgap, which is susceptible to temperature and radiation intensity changes. Previous studies have explained the temperature effect on the perovskite's bandgap using the theory developed for conventional semiconductors^{10,11}, which considers the thermal lattice expansion effect¹²⁻¹⁶ and the electron-phonon coupling effect¹⁷⁻²⁰. However, compared with conventional semiconductors, perovskites have soft and flexible structures²¹⁻²³ and can exhibit lattice distortions such as the octahedral tilting²⁴⁻²⁷ and the atom off-centering²⁸⁻³³. While both static distortions (the structure at equilibrium) at low temperatures^{24,25,34,35} and dynamic lattice vibrations at high temperatures^{21-23,36} have been shown to be essential for understanding the lattice dynamics in perovskites, their connection to the thermal evolution of the bandgap remains to be carefully examined.

In addition to the temperature effects, the photo-generated charge accumulation also impacts the bandgap. The state-filling near band edges leads to an increase in the optical bandgap, as described by the Burstein-Moss model, which provides a simple way to estimate the exciton effective mass μ (Refs.^{15,37-39}). The correlation and exchange interactions among photo-injected carriers can lead to a narrowing of the bandgap, a phenomenon known as bandgap renormalization^{40,41}. However, only the band-filling effect has been observed in fluence-dependent photoluminescence (PL) measurements so far, causing an overestimate of μ . Therefore, a clear demonstration of both the band-filling and the bandgap renormalization effects is highly desirable.

In this paper, we report on the temperature and photoexcited carrier density dependence of the bandgap in two hybrid perovskite thin films, $\text{MA}_{0.3}\text{FA}_{0.7}\text{PbI}_3$ and $\text{MA}_{0.3}\text{FA}_{0.7}\text{Pb}_{0.5}\text{Sn}_{0.5}\text{I}_3$ (abbreviated as Pb- and PbSn-perovskite, respectively), using PL and absorption spectroscopy. We chose to study these two compounds for two reasons: (1) the optimization of the organic cation mixing ratio stabilizes the lattice structure, making thermal expansion effects and structural phase transitions unimportant; (2) comparing the conventional pure-lead perovskite

with the mixed-lead-tin perovskite can identify critical aspects of the metal cation by examining the difference in their structures. On the application side, our PbSn-perovskite has achieved a record power conversion efficiency when implemented in an all-perovskite tandem solar cell^{2,42}. Understanding their bandgap's temperature and photocarrier dependence is essential for enhancing the power conversion efficiency and especially for advancing photovoltaic applications under extreme conditions (e.g., in space).

In our experiments, we observe strong temperature dependence and contrasting behavior of the bandgap between the two perovskites: the bandgap of the PbSn-perovskite shifts almost monotonically by 184 meV from 10 K to 340 K, whereas the bandgap of the Pb-perovskite shifts nonmonotonically with an overall change of only 2 meV in the same temperature range. By performing X-ray diffraction and hydrostatic pressure PL experiments, we find that both samples remain in the cubic phase at low temperatures and the thermal expansion effect only contributes up to ~10% of the bandgap change in our samples. Given their thermally-stable cubic structure, we propose that both static and dynamic lattice distortions are the origin of their unusual bandgap shifts with temperature based on first-principles calculations. In addition, we demonstrate both the bandgap renormalization and the band-filling effects for the first time in fluence-dependent PL measurements, providing a simple and relatively accurate way to determine exciton effective masses. Our study deepens the understanding of the fundamental bandgap and distortion properties in perovskite thin films and provides insights for further engineering of the electronic structure of this emerging class of semiconductors.

2. Results and Discussion

2.1. Cubic Phase Stabilization

We synthesized high-quality Pb- and PbSn-perovskite thin films based on our previously reported method⁴². Figure 1a presents a schematic of the atom distribution in the mixed FA-MA perovskites. Perovskites commonly undergo several structural phase transitions upon cooling, such as the cubic-to-tetragonal transition at 330 K and the tetragonal-to-orthorhombic transition

at 160 K in MAPbI₃ (Ref.⁵). Similar transitions also occur in FAPbI₃, which suffers from the spontaneous transitions from the α -phase (photoactive) to the δ -phase (non-photoactive) at room temperature and further to the tetragonal phase at 140 K (Ref.⁵). Although our samples have been found to be thermodynamically stable in the cubic phase at room temperature⁴², their structure at low temperatures remains unexplored. Previous studies of single-crystal FA_{0.7}MA_{0.3}PbI₃ have identified the cubic $Pm\bar{3}m \rightarrow$ tetragonal-II $P4/mbm \rightarrow$ tetragonal-III transition sequence based on the PL shifting curve and the single crystal XRD pattern change with temperature^{43,44}. However, the results were inconclusive regarding their low-temperature space group symmetry, and therefore are worth further investigation.

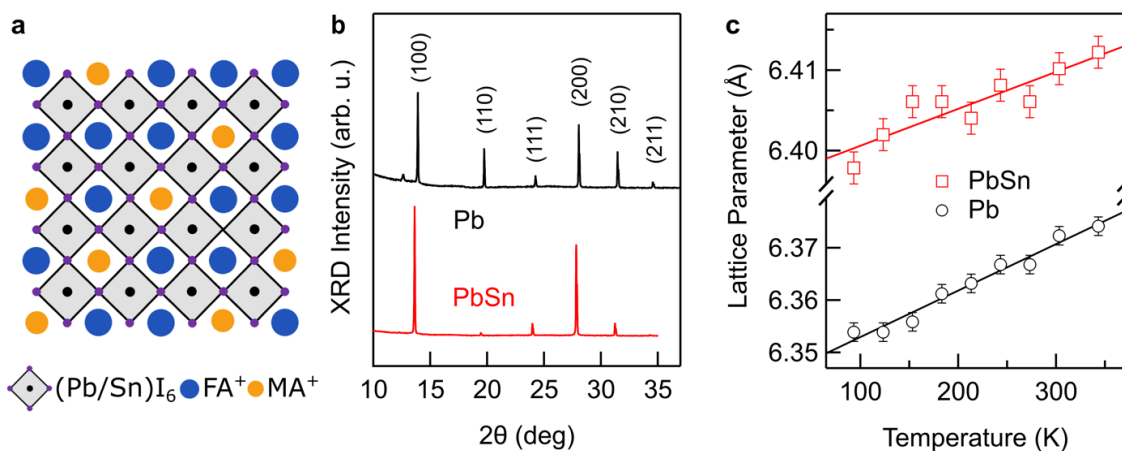


Figure 1. Structural properties of the Pb- and PbSn-perovskites. **a** Schematic representation of the atom distribution in mixed-cation perovskite films. **b** Powder X-ray diffraction (PXRD) patterns for the Pb- (black curve) and PbSn- (red curve) perovskites at 90 K. The Miller indices are labelled for each peak. The patterns show the cubic structure for both perovskites. **c** Temperature dependence of lattice parameters in the Pb- (black) and PbSn- (red) perovskites, extracted from PXRD peaks using Bragg's law. The solid lines represent linear fits to the data.

We performed powder X-ray diffraction (PXRD) measurements on the Pb- and PbSn-perovskites from 90 K to 340 K. In contrast to the previous study using single-crystal XRD spectroscopy⁴⁴, our PXRD patterns match with the cubic structure over the entire temperature range for both samples (only the 90 K data is shown in Figure 1b for simplicity; the entire temperature-dependent dataset and more details are included in Supporting Note 1). No abrupt change in the

diffraction peak intensities or angles is observed, and no additional peak broadening occurs upon cooling. Therefore, we expect long-range cubic symmetry for both our perovskites from 340 K down to 90 K.

The disappearance of phase transitions has also been observed in other cation-alloyed perovskites, such as the mixed methylammonium/dimethylammonium $\text{MA}_{0.79}\text{DMA}_{0.21}\text{PbBr}_3$ hybrid perovskites⁴⁵. Previous research has shown that the A-site cation in the ABX_3 perovskite structure directly affects the phase and thermal stabilities in three ways. First, the phase stability can be optimized by the Goldschmidt tolerance factor, defined as $t = (r_A + r_X)/[\sqrt{2}(r_B + r_X)]$, where r_A , r_B and r_X are the ionic radii in the A, B, and X sites, respectively. Partially substituting FA^+ in FAPbI_3 with the smaller-sized MA^+ and Cs^+ tunes the tolerance factor to the optimized cubic-phase value ($0.9 < t < 1$) (Refs. ^{4,5}). Second, since the structural transitions are initiated by the collective tilting of the $[\text{BX}_6]^{4-}$ octahedra upon cooling, cation mixing can introduce frustrated electric dipoles that suppress the long-range ordering of the $[\text{BX}_6]^{4-}$ octahedra. This results in the stabilization of the cubic phase even at low temperatures⁴⁵. Third, cation mixing may help to relax the crystal strain that builds up during the phase transition^{3,4}. Considering that our XRD results are inconsistent with previous single-crystal studies^{43,44}, it is possible that the potential strain relaxation at crystallite grain boundaries also contributes to the phase stabilization in our thin film samples.

In addition to identifying the structure, the volumetric thermal expansion coefficient (α_V) can be inferred from the gradual shift of the PXRD peak angles with increasing temperature. α_V of the Pb- and PbSn-perovskites are $5.6 \times 10^{-5} \text{ K}^{-1}$ and $2.9 \times 10^{-5} \text{ K}^{-1}$, respectively (Figure 1c). These values are significantly smaller than those of perovskites containing single organic cations²⁹ (e.g., α_V in the Pb-perovskite is smaller than that in $\alpha\text{-FAPbI}_3$ and MAPbI_3 by a factor of two) and the mixed-cation perovskite single crystal $\text{MA}_{0.5}\text{FA}_{0.5}\text{PbI}_3$ (Ref.⁴⁴), which again signifies the enhanced structural stability of our samples. However, we have to be aware that α_V of the Pb- and PbSn-perovskites are one order of magnitude higher than those of conventional semiconductors such as Si and GaAs (Ref.⁴⁶), whose covalent bonds are more rigid. The relatively soft and flexible

perovskite lattice makes them prone to distorted bond angles while maintaining their cubic structure. The effects of thermal expansion and lattice distortion on bandgap will be discussed in detail later.

2.2. Bandgap Shifts with Temperature

To measure the temperature dependence of the bandgap, we record the steady-state PL spectra of the Pb- and PbSn-perovskites from 10 K to 340 K, as shown in Figure 2a,b. The PL peak energy (white circles) shows contrasting temperature dependence between the Pb- and PbSn-perovskites. In the Pb-perovskite, the PL shifts non-monotonically as the temperature increases, with blueshifts below 100 K and above 200 K and redshifts in between, leading to a small overall energy increase of 2 meV in the entire measured temperature range. In the PbSn-perovskite, by contrast, the PL monotonically blueshifts with increasing temperature, and a large overall energy increase of 184 meV is observed in the same temperature range. Additionally, below 70 K, where the bandgap shifts approximately linearly with the temperature, the PbSn-perovskite shows a larger shifting rate of 0.61 meV K⁻¹ than that of the Pb-perovskite (0.25 meV K⁻¹). From 290 K to 340 K, the shifting rate for the Pb- and PbSn-perovskites is 0.46 meV K⁻¹ and 0.72 meV K⁻¹, respectively.

The PL energy shift is attributed to the temperature dependence of the bandgap, as confirmed by the absorbance spectra shown in Figure 2c,d. The brown region tracks the absorption onset, and the bandgap values extracted from the Elliot model and the Tauc plot are plotted with black circles (see Supporting Note 3 for details). The bandgap has the same shifting trends as the PL peak energy, but is at a slightly higher energy due to the exciton binding energy⁴⁷⁻⁵¹ and the Stokes shift⁵², etc. The bandgap blueshift with increasing temperature is an unusual behavior compared with conventional semiconductors, but is ubiquitous in metal halide perovskites. In particular, the large monotonic blueshift of the bandgap seems to be a unique feature in tin-based perovskites^{12,53}. In our phase-stabilized Pb-perovskite, a change from blue to red shift in the bandgap is observed between 100 K and 200 K while the structure remains in the cubic phase,

indicating that the nonmonotonic bandgap shift cannot be ascribed to phase transitions, as suggested by previous work¹³.

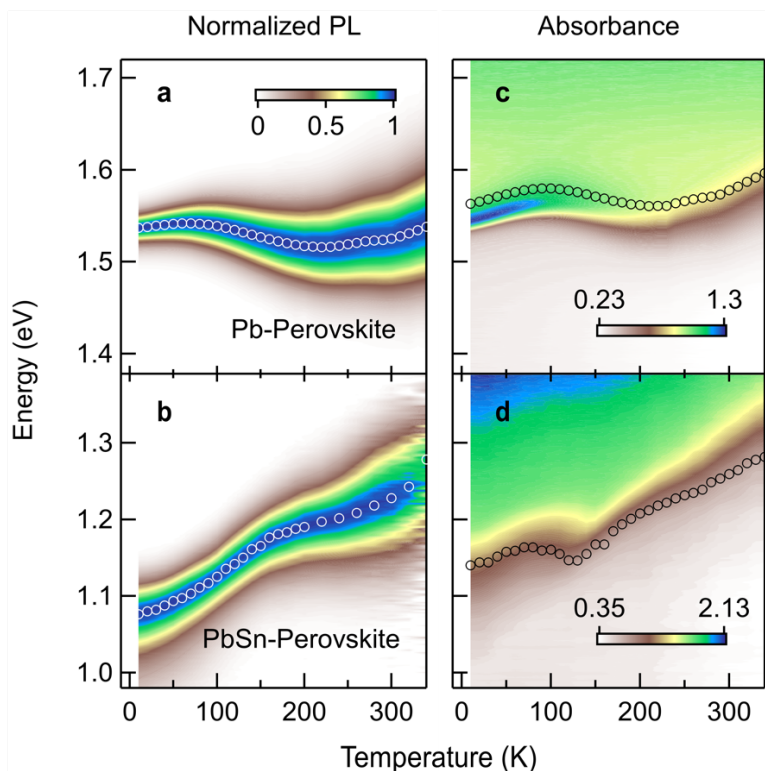


Figure 2. Bandgap shift with temperature. Color plots of the normalized PL (a,b) and absorbance (c,d) spectra, respectively, for the Pb- and PbSn-perovskites from 10 to 340 K. The white open circles in the PL color plots label the PL peak energies and the black circles in the absorbance plots represent the bandgap values extracted from the Elliot model fit (for the Pb-perovskite) and the Tauc plot analysis (for the PbSn-perovskite) of the absorbance spectra (Figure S4, Supporting Information). Error bars are smaller than the markers.

2.3. Estimation of Thermal Expansion Effect

Previous analyses of the bandgap shift with temperature in hybrid metal halide perovskites ascribed substantial importance to the thermal expansion effect, both in pure-lead and pure-tin perovskites^{12,13,16}, due to the large thermal expansion coefficients of the single-organic-cation samples. To make a more accurate estimate of the lattice dilation effect in our samples, we perform hydrostatic pressure PL experiments to measure the pressure coefficient of the bandgap

dE_g/dP up to 1.2 GPa at room temperature. As shown in Figure 3, the bandgap shrinks upon increasing pressure in both samples. dE_g/dP is measured to be -41 meV GPa^{-1} and -82 meV GPa^{-1} for the Pb- and PbSn-perovskites, respectively.

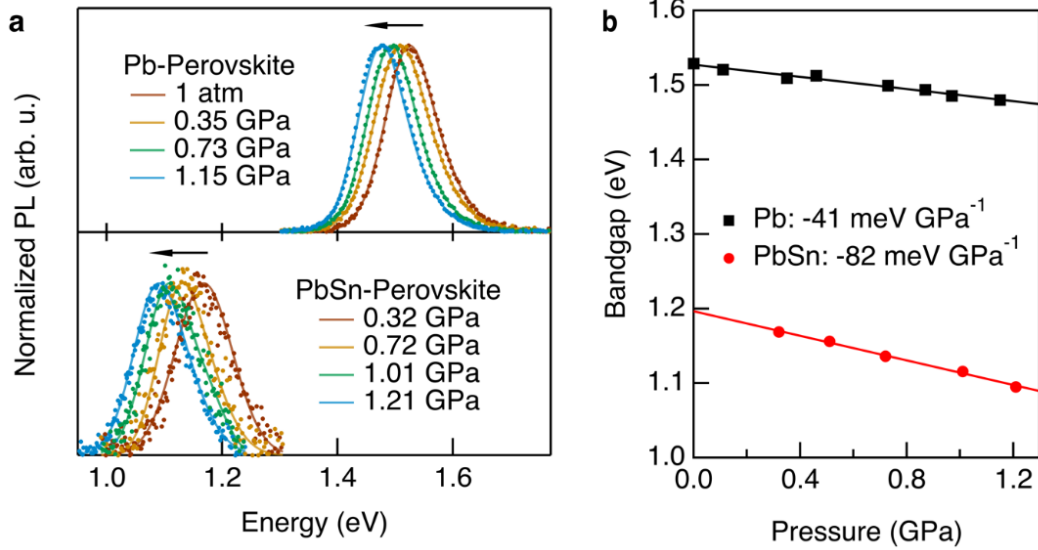


Figure 3. Bandgap redshift upon compression at room temperature. **a** PL spectrum with increasing pressures measured in situ in a diamond anvil cell apparatus. The black arrow indicates the evolution of the PL spectra upon compression. **b** Pressure dependence of bandgap deduced from the center of the emissions. Bandgap pressure coefficients are obtained from the slopes of the linear fits and are included in the legend.

The thermal expansion effect on the bandgap is calculated as⁵⁴ $(\partial E_g/\partial T)_{TE} = -\alpha_V B_0 (dE_g/dP)$, where α_V is the volumetric thermal expansion coefficient and B_0 is the bulk modulus. The pressure coefficients of the bandgap for our samples are comparable to the literature values for FAPbI_3 and MAPbI_3 perovskites^{54,55}. Because in situ synchrotron PXRD experiments under pressure showed similar values of the bulk moduli among all types of iodide perovskites (Table S1, Supporting Information), we use the largest value of $B_0 = 13.6 \text{ GPa}$ found in the literature^{56,57} to make an estimate. Then $(\partial E_g/\partial T)_{TE}$ is calculated to be 0.031 meV K^{-1} and 0.033 meV K^{-1} for the Pb- and PbSn-perovskites, respectively, which are significantly smaller than the measured values of 0.25 meV K^{-1} and 0.61 meV K^{-1} at temperatures below 70 K, and 0.46 meV K^{-1}

and 0.72 meV K^{-1} at temperatures above 290 K. Therefore, thermal lattice expansion plays a minor role in the bandgap shift of our phase-stabilized perovskites with temperature. Other structural changes are likely responsible for the anomalous bandgap shift. We use numerical methods to analyze these effects in the next section.

2.4. Effects of Lattice Distortions on Bandgap

The Pb- and PbSn-perovskites, although stabilized in the cubic phase, possess flexible corner-sharing $[\text{PbI}_6]^{4-}$ (or $[\text{SnI}_6]^{4-}$) octahedral frames that are susceptible to distortions. For example, neutron powder diffraction experiments on the tetragonal phase of MAPbI_3 have measured the statically distorted I-Pb-I bond angle to be as small as 157° at low temperatures^{34,35}, with 180° representing the undistorted angle. In addition, strong dynamic distortions at high temperatures have been revealed by molecular dynamics and density functional theory (DFT)^{22,36,58}, and X-ray and neutron scattering experiments^{21,23}. Notably, the dynamic local symmetry breaking caused by highly anharmonic phonons has been revealed in the high-temperature cubic perovskite lattice^{21,23,59}. While our PXRD results confirm the preservation of perfect long-range cubic symmetry down to low temperatures, local distortions can still exist. We suspect that the combined effects of static and dynamic lattice distortions with temperature are the most likely origin of the unusual bandgap shifts in our phase-stabilized samples.

To consider appropriate distortion modes in our systems, we first rule out the tilting of the rigid $[\text{PbI}_6]^{4-}$ (or $[\text{SnI}_6]^{4-}$) octahedra for the following reasons: (1) static tilting breaks the cubic symmetry, inconsistent with the observed PXRD results; (2) the activation of more dynamic tilting modes is associated with negative thermal lattice expansion and a positive gap pressure coefficient²⁷, which are opposite in sign to those observed in our Pb- and PbSn-perovskites.

Instead, we examine the effects of the distorted I-Pb-I bond angle with a fixed overall lattice parameter, as depicted in the inset of Figure 4a. This distortion mode (such as the lead atom off-centering effect) has been studied in perovskites before and is sometimes termed “emphanisis” in the literature^{28–33}. We present a numerical analysis of the unusual bandgap shifts based on this

type of lattice distortion, consisting of two parts: (1) the influence of the lattice distortions on the perovskite band structure, and (2) how (static and dynamic) lattice distortions change with rising temperature.

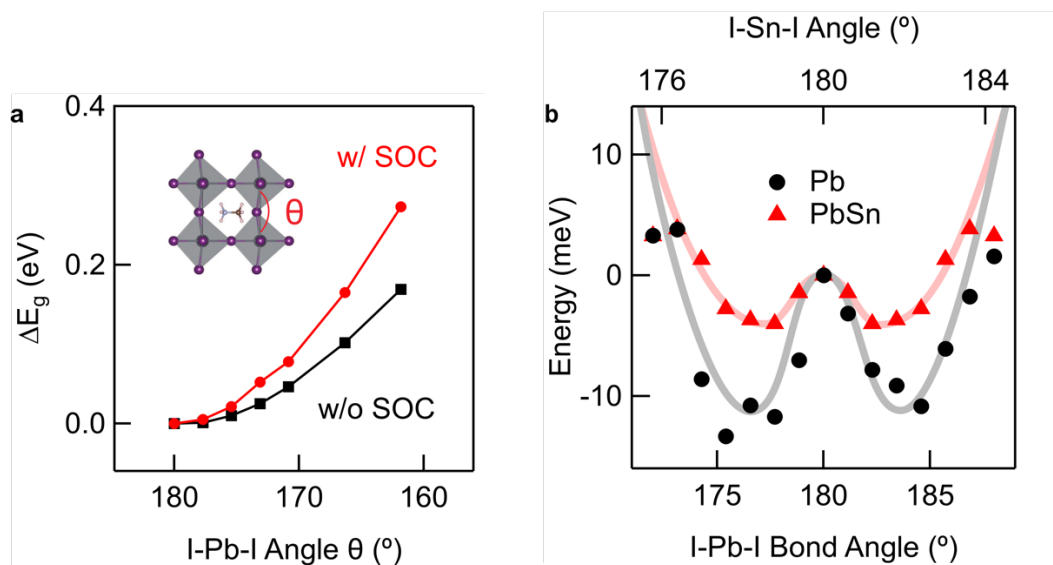


Figure 4. Results of first-principles calculations. **a** Bandgap enhancement by lattice distortions represented by the I-Pb-I bond angle θ (inset, the distortion is applied to the iodine atoms) with (w/) or without (w/o) the SOC effect. **b** Double-well shaped potential of the Pb- and PbSn-perovskites versus the distortion angle. The data for the PbSn-perovskite is extracted from Figure S9 in Supporting Information. The lines in **b** are guides to the eye showing the double well shape of the total energy.

Band structures of the Pb-perovskite calculated using DFT are depicted in Figure S7 (Supporting Information). Because the electronic states near the Fermi level are mainly contributed by the inorganic component, we take the representative composition of MAPbI_3 in our calculations for simplicity, while using the cubic lattice structure and lattice parameter from the PXRD measurements (FAPbI_3 shows similar results). The conduction band minimum (CBM) corresponds to an anti-bonding state mainly formed by the p orbitals of Pb and I, and the valence band maximum (VBM) corresponds to an anti-bonding state mainly formed by the s orbital of Pb and the p orbital of I.

The strong dependence of the bandgap on the lattice distortion angle is plotted in Figure 4a. The bandgap enhancement reaches hundreds of meV, both with and without spin-orbit coupling (SOC). The lattice distortions denoted in the inset of Figure 4a lead to increased bond lengths, reducing the orbital overlap integrals in the Pb-I bonds. Because antibonding orbitals are repulsively formed with an energy increase, the antibonding CBM and VBM states shift downwards in energy when the overlap reduction occurs with a weaker repulsion. However, the VBM shift is larger than the CBM shift because the Pb *s* orbital of the VBM is more localized than the Pb *p* orbital of the CBM and hence more sensitive to the bond stretching.

In addition to the lattice distortions considered in Figure 4a, we also study another kind of lattice distortions that displaces iodine atoms away from the equilibrium position along the Pb-I bond direction and find similar enhancement of bandgap by lattice distortion as (Figure S6, Supporting Information). Additionally, Figure 4a shows a greater enhancement of the bandgap when SOC is included than when it is not included, which is due to the reduction in the SOC splitting energy with increasing distortion caused by the crystal field effects (see details in Supporting Note 7). Overall, the lattice distortions affect both the orbital overlap and the SOC splitting, leading to a large increase in the bandgap.

To reveal the relationship between lattice distortions and temperature, we calculate the total energy of the system at different distortion angles for both the Pb- and PbSn-perovskites in Figure 4b. The potential energy curves show double-well shapes, nearly symmetric about the undistorted 180° bond angle. The two perovskites have different potential well depths (-11 meV for the Pb-perovskite compared to -4 meV for the PbSn-perovskite) and different distortion angles at the well bottoms (176° and 184° for the Pb-perovskite compared to 178° and 182° for the PbSn-perovskite).

The double-well potential energy curves indicate that the perovskite prefers the distorted angle at the minimum energy at low temperatures. However, as the temperature increases, the lattice structure gradually moves away from the distorted angle and becomes the perfect cubic

structure at room temperature. This change in the equilibrium structure reduces the “static” lattice distortion with increasing temperature, thereby shrinking the bandgap. This is supported by a previous study on CsSnI_3 (Ref. ⁵⁹), which showed that the angles of the double well potential minima shift towards the undistorted angle and the well depth decreases as the thermal vibration is enhanced with increasing temperature.

In addition to “static” deformation, thermally-induced lattice vibrations lead to “dynamic” structural distortions. Previous molecular dynamic simulations of MAPbI_3 have shown strong spatial fluctuations of the iodine atoms⁶⁰, evidencing significant dynamic distortions in the high-temperature cubic phase. The anharmonic double-well potential has also been suggested to be responsible for the soft phonon modes and the corresponding structural instability at high temperatures^{21–23}. Because the lattice vibration amplitude generally grows with temperature, the enhanced dynamic distortions consequently cause an enhanced bandgap. The overall bandgap change with temperature would therefore depend on both the static and dynamic distortion changes.

The PbSn -perovskite likely has a small static but large dynamic lattice distortion change with temperature. Due to its small distortion angle, a small amount of thermal energy can excite the system, resulting in a minor static deformation change with increasing temperature. Additionally, because of the shallow potential well depth (4 meV equivalent to ~ 46 K), the PbSn -perovskite is prone to stronger lattice vibrations and therefore a larger dynamic distortion change. This agrees well with the observation of the much larger bandgap shift rate in the PbSn -perovskite (0.61 meV K^{-1}) than the Pb -perovskite (0.25 meV K^{-1}) below 70 K (Figure 2). As the temperature increases, the dynamic distortions quickly overcome the static counterpart and dominate, causing the overall monotonic blueshift of the bandgap (Figure 2b,d).

In contrast, the deeper potential well in the Pb -perovskite (11 meV, ~ 126 K) suggests that the system oscillates around one of the distorted angles of the energy minimum at low temperatures and the change of static distortion is very small. Therefore, the bandgap blueshifts due to the

enhanced thermal vibrations. In the intermediate temperature range, we speculate that the bandgap redshift between 100 K and 200 K (Figure 2a,c) is due to the substantial reduction of the large static distortion. Note that similar bandgap blue-to-red shift turnover of other lead-based perovskites in the intermediate temperature range has been attributed to the structural phase transitions^{13,43}, which clearly fails to describe our samples due to their stabilized cubic structures. As the temperature increases further, the local static distortion disappears due to the fast rotation of the A-site cations, and the dynamic distortions regain dominance, leading to an expansion of the bandgap. The moderate overall increase of the bandgap in the Pb-perovskite is due to the compensation between the static and dynamic contributions from 10 K to 340 K.

2.5. Bandgap Renormalization and Band-filling Effects

In addition to the temperature dependence, energy shifts of the PL emission are also observed as the excitation density changes. Figure 5a,b shows the shift of PL spectra at 10 K as a function of the pump fluence for the Pb- and PbSn-perovskites (from 3 nJ cm⁻² to 5 μJ cm⁻² for the Pb-perovskite, and from 129 nJ cm⁻² to 15 μJ cm⁻² for the PbSn-perovskite). The fluence can be converted to photocarrier density n (Supporting Note 8), and the different measurement ranges for the two samples are determined by the detector sensitivity and laser output power (see Experimental Section).

As shown in Figure 5a,c, the Pb-perovskite shows a redshift of the emission under low excitation fluences (up to $n \sim 10^{16}$ cm⁻³) followed by a blueshift upon further increasing the pump fluence. In the PbSn-perovskite, however, a monotonic blue shift is observed with increasing photocarrier density (n from 10^{16} to 10^{18} cm⁻³) (Figure 5b,d). We attribute the PL blueshift to the band filling effect and the redshift to the bandgap renormalization (BGR) effect. The BGR has been observed in perovskites only by transient absorption spectroscopy^{61,62} but not with linear optical methods until now.

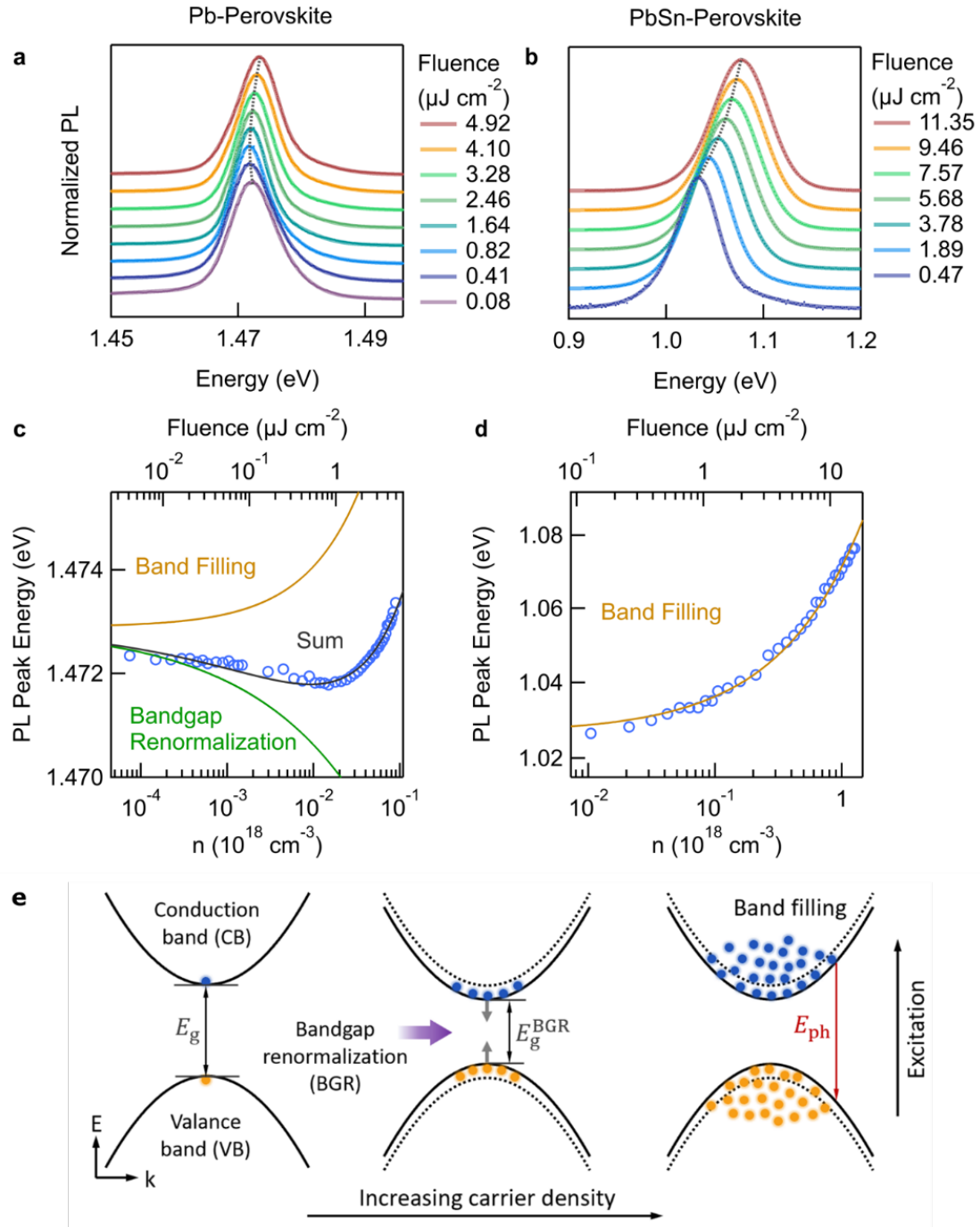


Figure 5. Band filling and bandgap renormalization effects. **a** Normalized PL spectra of the Pb-perovskite with excitation fluence increasing from 3 nJ cm^{-2} to $5 \mu\text{J cm}^{-2}$ at 10 K, showing a small redshift at low fluence and then a blueshift at high fluence. **b** Fluence-dependent PL spectra of the PbSn-perovskite with excitation fluence from 129 nJ cm^{-2} to $15 \mu\text{J cm}^{-2}$, showing a large and monotonic blueshift. Shifts of the PL peak energy as a function of the excitation fluence for the Pb- (**c**) and PbSn- (**d**) perovskites, respectively. The corresponding carrier densities (n) are indicated in the bottom axis. Blue circles represent the

experimental data. The brown line shows the band filling effect ($E_g^0 + \Delta E_g^{\text{BM}}$), the green line shows the bandgap renormalization effect ($E_g^0 + \Delta E_g^{\text{BGR}}$), and the black line is a sum of both ($E_g^0 + \Delta E_g^{\text{BM}} + \Delta E_g^{\text{BGR}}$), where E_g^0 is the intrinsic bandgap that does not depend on n . **e** Schematic of the bandgap renormalization and band filling effects.

The band filling effect, also called the Burstein-Moss shift^{38,39}, has been widely observed in perovskites by transient absorption³⁷ and PL spectroscopy¹⁵. As schematically shown in Figure 5e, a relatively low density of photoinduced carriers can fill the bands to an appreciable depth and thus can widen the effective bandgap, inducing optical transitions at energies higher than the fundamental bandgap. Because of the similar effective mass of electrons and holes in metal trihalide perovskites⁶³, both carriers contribute to the state filling. The magnitude of the bandgap widening due to the band filling effect can be modelled by the Burstein-Moss expression⁶⁴ $\Delta E_g^{\text{BM}} = \hbar^2(3\pi^2n)^{2/3}/2\mu$, where \hbar is the reduced Plank constant and μ is the reduced effective mass of excitons.

Although the band-filling effect in the perovskites was detected first by the shift in the absorption edge upon photoinjection³⁷, the large PL blue shift has been observed in FASnI₃ and has been attributed to the slow hot carrier cooling¹⁵. The possible phonon bottleneck effect⁶² makes the PL emission energy mostly contributed by the recombination of the electrons and holes near their quasi Fermi levels, whose difference is therefore a good representation of the optical gap.

Besides the intuitive filling process, optical excitations can generate a dense electron-hole plasma where many-body effects take place. Carriers with the same charge repel each other by the Coulomb interaction, and the Pauli exclusion principle further separates carriers with the same spin. The correlation and exchange interaction between the carriers cause screening in the electron-hole system and renormalizes their self-energies, which narrows the bandgap^{40,41} (Figure 5e).

The BGR effect has been investigated in-depth in heavily doped semiconductor systems. A phenomenological expression⁶⁵ describes the BGR energy shift as $\Delta E_g^{\text{BGR}} = -\gamma n^{1/3}$, where γ is the BGR coefficient related to the static dielectric constant of the material. The total change in the bandgap can be defined as a combination of the two contributions $\Delta E_g = \Delta E_g^{\text{BM}} + \Delta E_g^{\text{BGR}}$, yielding a redshift of the optical bandgap at low fluences and then a blueshift at high fluences.

Figure 5c shows an excellent description of the Pb-perovskite data over the entire range of excitation intensities when both the band-filling and BGR effects are considered. From the fit, we can estimate $\mu = 0.146(6)m_0$ for the Pb-perovskite, similar to that of $0.1m_0$ determined by high-field magnetoabsorption measurements⁴⁷, where m_0 is the free electron mass. We also obtain a BGR coefficient of $\gamma = 1.05(5) \times 10^{-8}$ eV cm, which is comparable to the values in typical inorganic semiconductors, such as 4.27×10^{-8} eV cm in Si-doped GaN (Ref.⁶⁶), 2.25×10^{-8} eV cm in n-type InP (Ref.⁶⁷), and 1.2×10^{-8} eV cm in lead-iodide perovskites extracted by transient absorption spectroscopy⁶². Previous fluence-dependent studies^{15,37} for the Pb-perovskites injected photocarriers higher than $n \sim 10^{16}$ cm⁻³, obtaining a much higher exciton effective mass of $0.33m_0$; our work reveals that it is critical to cover very low excitation densities to successfully account for the BGR effect in the effective mass calculation (a comparison with one excluding the BGR effect is demonstrated in Supporting Note 9).

In the PbSn-perovskite, the large dark noise of the InGaAs detector limits our measurement range of photoexcitation densities to $n \sim 10^{16}$ cm⁻³ and above. This restricts the PL detection for the PbSn-perovskite to the fluence range where band filling is dominant. In Figure 5d, the PbSn-perovskite data can be fit perfectly with the Burstein-Moss expression, confirming the dominance of band filling over the entire fluence range. The obtained $\mu = 0.081(1)m_0$ agrees well with the previous report of $0.12m_0$ at 24 K in FASnI₃ obtained from power-dependent PL spectra¹⁵ and the calculation result of $0.075m_0$ in mixed-PbSn perovskites⁶³.

3. Conclusion

In summary, we report on the temperature and photoexcited carrier density dependence of the bandgap in two phase-stabilized perovskite thin films $\text{MA}_{0.3}\text{FA}_{0.7}\text{PbI}_3$ and $\text{MA}_{0.3}\text{FA}_{0.7}\text{Pb}_{0.5}\text{Sn}_{0.5}\text{I}_3$. In stark contrast to previous studies, we have revealed that the temperature-dependent bandgap shifts in our samples cannot be explained by the thermal lattice expansion and structural phase transitions, due to their small lattice expansion and stabilized cubic structure. Instead, using first-principles simulations, we have proposed that the unusual bandgap shift with temperature originates from static local distortions at low temperatures and their competition with dynamic lattice vibrations. By measuring fluence-dependent PL down to a very low excitation density (10^{14} cm^{-3}), we have demonstrated the BGR effect for the first time in addition to the band-filling effect, and have shown that accounting for the BGR effect leads to a more accurate estimation of the exciton effective mass. Our findings clarify and provide a deeper understanding of the optical bandgap shifts with temperature and excitation intensity in perovskite thin films, and are instructive for future applications and designs of perovskite-based optoelectronic devices.

4. Experimental Section

Perovskite Thin Film Preparation

The samples in this study are solution-processed $\text{MA}_{0.3}\text{FA}_{0.7}\text{PbI}_3$ and $\text{MA}_{0.3}\text{FA}_{0.7}\text{Pb}_{0.5}\text{Sn}_{0.5}\text{I}_3$ perovskite thin films (hereafter referred to as Pb- and PbSn-perovskite). The PbSn-perovskite was prepared using a tin-reduced precursor solution strategy to effectively prevent the oxidation of Sn^{2+} to Sn^{4+} . This synthesis strategy, which is described in Ref.⁴², significantly reduces both the trap density and the hole density by a factor of two compared to a control sample. The thicknesses of the Pb- and the PbSn-perovskite samples are $1.0 \mu\text{m}$ and $1.2 \mu\text{m}$, respectively (see Figure S10, Supporting Information).

X-Ray Diffraction Spectroscopy

Crystal structure and lattice parameters were determined by X-ray diffraction using a Bruker D8 Advanced diffractometer with $\text{Cu K}\alpha$ radiation (wavelength: 1.54 \AA). Samples were transported

to a liquid nitrogen-cooled stage under vacuum and operated in a temperature range of 90 K to 340 K.

Temperature-Dependent Absorption and Photoluminescence

The thin films were mounted on a cold finger of a closed-loop helium cryostat under vacuum to vary the temperature from 10 K to 340 K. For absorption measurements, a stabilized quartz-tungsten lamp was used as the white light source. The beam was spatially limited by an iris, collimated, and then focused on the sample with a 50 mm focal length lens. The transmitted light was collected by a multi-mode fiber coupled to the entrance slit of a Czerny-Turner spectrometer. The spectra were recorded by a thermoelectrically cooled EMCCD (detection range: 250-1050 nm) for the Pb-perovskite and an InGaAs single-point detector (800-2500 nm) for the PbSn-perovskite. For temperature-dependent PL measurements, two continuous-wave diode lasers (633 nm and 785 nm for the Pb- and the PbSn-perovskites, respectively) were used as the excitation sources. The setups were similar to our previous study⁶⁸.

Fluence-Dependent Photoluminescence

The fluence-dependent PL was measured with an 80-MHz mode-locked Ti:Sapphire laser for accurate calculations of the photoinjected carrier density. The beam passed through an acoustic-optical pulse selector with a 20:1 division ratio to reduce the thermal effect and achieve a full recovery from the excitation. The Pb- and PbSn-perovskites were excited at the wavelength of 720 nm and 785 nm, respectively. The maximum power on the PbSn-perovskite is larger than that on the Pb-perovskite because the peak power output from the Ti:Sapphire laser is located at ~805 nm. The laser power incident on the sample was adjusted by a set of variable neutral density filters. Both the excitation light illumination and the PL collection were on the thin-film side rather than the substrate side to avoid self-absorption effect. Notably, the EMCCD camera provides exceptional sensitivity and noise performance (~single electron) compared to the InGaAs detector (~ 10^3 electrons). Therefore, only the PL of the Pb-perovskite can be detected with a laser fluence down to 3 nJ cm^{-2} .

In Situ High-Pressure Photoluminescence

High-pressure experiments were carried out using a symmetric diamond anvil cell apparatus. The samples were scraped off from the substrates and loaded into a 250 μm -diameter chamber, which was constructed from a T301 steel gasket and pre-indented into a thickness of 40 μm . Mineral oil was used as the pressure-transmitting medium. Several ruby balls with diameters of approximately 30 μm were placed in the sample chamber. The pressure calibration was determined by the ruby fluorescence method. A diode laser with an excitation wavelength of 633 nm was used for all luminescence experiments. The beam was focused onto the sample using a 20 \times long working distance objective.

Computation Methods

DFT calculations were performed with the Vienna *ab initio* simulation package⁶⁹ using the projector-augmented wave method together with the plane-wave basis with an energy cutoff of 430 eV. The Perdew-Burke-Ernzerhof exchange-correlation functional⁷⁰ was applied. The materials studied by experiments have mixed organic components, which are difficult to handle in DFT calculations. Since the A-site molecule has minor influence on electronic states near the Fermi level, we simplified the system from the mixed A-site to pure MA and include the influence of FA by adding structural constraints. That is, the structure was artificially kept in cubic phase during relaxation and the experimental lattice constants from our XRD measurements were employed, which were fixed to be 6.375 Å for MAPbI_3 and 6.410 Å for $\text{MAPb}_{0.5}\text{Sn}_{0.5}\text{I}_3$. The MA molecule was aligned along the [100] direction, as recommended by previous work³⁴. $\text{MAPb}_{0.5}\text{Sn}_{0.5}\text{I}_3$ was simulated by doubling the unit cell along the [100] direction and replacing one Pb with Sn. Structural relaxation was performed with fixed lattice constants, using a force convergence criterion of 10^{-2} eV Å⁻¹. The k-points grids were set as $4 \times 4 \times 4$ for MAPbI_3 and $2 \times 2 \times 2$ for $\text{MAPb}_{0.5}\text{Sn}_{0.5}\text{I}_3$ for structural relaxation, which were increased to $8 \times 8 \times 8$ for self-consistent calculations. A van der Waals correction was introduced by the DFT-D3 method⁷¹ with the Becke-Jonson damping⁷².

Acknowledgements

Samples were prepared at Nanjing University. All optical measurements and first-principles calculations were performed at Tsinghua University. L.Y. acknowledges the support from the National Key R&D Program of China (Grant Nos. 2020YFA0308800 and 2021YFA1400100) and the National Natural Science Foundation of China (Grant Nos. 12074212). Y.X. was supported by the National Key R&D Program of China (2018YFA0307100 and 2018YFA0305603) and the National Natural Science Foundation of China (12025405 and 11874035). The work of H.T. was supported by the National Natural Science Foundation of China (Grant Nos. 61974063 and U21A2076). H.Z. was also supported by funds from the University of Toronto.

Competing interests

The authors declare no competing interests.

Reference

1. Wang, R. *et al.* Prospects for metal halide perovskite-based tandem solar cells. *Nat. Photonics* **15**, 411–425 (2021).
2. Gu, S. *et al.* Tin and Mixed Lead–Tin Halide Perovskite Solar Cells: Progress and their Application in Tandem Solar Cells. *Advanced Materials* **32**, 1907392 (2020).
3. Lee, J.-W., Tan, S., Seok, S. I., Yang, Y. & Park, N.-G. Rethinking the A cation in halide perovskites. *Science* **375**, eabj1186 (2022).
4. Byranvand, M. M. *et al.* Recent Progress in Mixed A-Site Cation Halide Perovskite Thin-Films and Nanocrystals for Solar Cells and Light-Emitting Diodes. *Advanced Optical Materials* **10**, 2200423 (2022).
5. Liu, X. *et al.* Stabilization of photoactive phases for perovskite photovoltaics. *Nat Rev Chem* 1–18 (2023) doi:10.1038/s41570-023-00492-z.
6. Jeon, N. J. *et al.* Compositional engineering of perovskite materials for high-performance solar cells. *Nature* **517**, 476–480 (2015).
7. Rajagopal, A., Stoddard, R. J., Hillhouse, H. W. & Jen, A. K.-Y. On understanding bandgap bowing and optoelectronic quality in Pb–Sn alloy hybrid perovskites. *J. Mater. Chem. A* **7**, 16285–16293 (2019).
8. Hao, F., Stoumpos, C. C., Chang, R. P. H. & Kanatzidis, M. G. Anomalous Band Gap Behavior in Mixed Sn and Pb Perovskites Enables Broadening of Absorption Spectrum in Solar Cells. *J. Am. Chem. Soc.* **136**, 8094–8099 (2014).

9. Eperon, G. E. *et al.* Perovskite-perovskite tandem photovoltaics with optimized band gaps. *Science* **354**, 861–865 (2016).
10. Lautenschlager, P., Allen, P. B. & Cardona, M. Temperature dependence of band gaps in Si and Ge. *Phys. Rev. B* **31**, 2163–2171 (1985).
11. Gopalan, S., Lautenschlager, P. & Cardona, M. Temperature dependence of the shifts and broadenings of the critical points in GaAs. *Phys. Rev. B* **35**, 5577–5584 (1987).
12. Yu, C. *et al.* Temperature dependence of the band gap of perovskite semiconductor compound CsSnI₃. *Journal of Applied Physics* **110**, 063526 (2011).
13. Dar, M. I. *et al.* Origin of unusual bandgap shift and dual emission in organic-inorganic lead halide perovskites. *Science Advances* **2**, e1601156 (2016).
14. Wright, A. D. *et al.* Electron–phonon coupling in hybrid lead halide perovskites. *Nat Commun* **7**, 11755 (2016).
15. Fang, H.-H., Adjokatse, S., Shao, S., Even, J. & Loi, M. A. Long-lived hot-carrier light emission and large blue shift in formamidinium tin triiodide perovskites. *Nat Commun* **9**, 243 (2018).
16. Francisco-López, A. *et al.* Equal Footing of Thermal Expansion and Electron–Phonon Interaction in the Temperature Dependence of Lead Halide Perovskite Band Gaps. *J. Phys. Chem. Lett.* **10**, 2971–2977 (2019).
17. Saidi, W. A., Poncé, S. & Monserrat, B. Temperature Dependence of the Energy Levels of Methylammonium Lead Iodide Perovskite from First-Principles. *J. Phys. Chem. Lett.* **7**, 5247–5252 (2016).
18. Tilchin, J. *et al.* Hydrogen-like Wannier–Mott Excitons in Single Crystal of Methylammonium Lead Bromide Perovskite. *ACS Nano* **10**, 6363–6371 (2016).

19. Saran, R., Heuer-Jungemann, A., Kanaras, A. G. & Curry, R. J. Giant Bandgap Renormalization and Exciton–Phonon Scattering in Perovskite Nanocrystals. *Advanced Optical Materials* **5**, 1700231 (2017).
20. Saidi, W. A. & Kachmar, A. Effects of Electron–Phonon Coupling on Electronic Properties of Methylammonium Lead Iodide Perovskites. *J. Phys. Chem. Lett.* **9**, 7090–7097 (2018).
21. Beecher, A. N. *et al.* Direct Observation of Dynamic Symmetry Breaking above Room Temperature in Methylammonium Lead Iodide Perovskite. *ACS Energy Lett.* **1**, 880–887 (2016).
22. Marronnier, A. *et al.* Structural Instabilities Related to Highly Anharmonic Phonons in Halide Perovskites. *J. Phys. Chem. Lett.* **8**, 2659–2665 (2017).
23. Lanigan-Atkins, T. *et al.* Two-dimensional overdamped fluctuations of the soft perovskite lattice in CsPbBr₃. *Nat. Mater.* **20**, 977–983 (2021).
24. Amat, A. *et al.* Cation-Induced Band-Gap Tuning in Organohalide Perovskites: Interplay of Spin–Orbit Coupling and Octahedra Tilting. *Nano Lett.* **14**, 3608–3616 (2014).
25. Prasanna, R. *et al.* Band Gap Tuning via Lattice Contraction and Octahedral Tilting in Perovskite Materials for Photovoltaics. *J. Am. Chem. Soc.* **139**, 11117–11124 (2017).
26. Klarbring, J. Low-energy paths for octahedral tilting in inorganic halide perovskites. *Phys. Rev. B* **99**, 104105 (2019).
27. Adams, D. J. & Churakov, S. V. Classification of perovskite structural types with dynamical octahedral tilting. *IUCrJ* **10**, 309–320 (2023).

28. Worhatch, R. J., Kim, H., Swainson, I. P., Yonkeu, A. L. & Billinge, S. J. L. Study of Local Structure in Selected Organic–Inorganic Perovskites in the $Pm\bar{3}m$ Phase. *Chem. Mater.* **20**, 1272–1277 (2008).
29. Fabini, D. H. *et al.* Reentrant Structural and Optical Properties and Large Positive Thermal Expansion in Perovskite Formamidinium Lead Iodide. *Angewandte Chemie* **128**, 15618–15622 (2016).
30. Laurita, G., Fabini, D. H., Stoumpos, C. C., Kanatzidis, M. G. & Seshadri, R. Chemical tuning of dynamic cation off-centering in the cubic phases of hybrid tin and lead halide perovskites. *Chem. Sci.* **8**, 5628–5635 (2017).
31. Kontos, A. G. *et al.* Dynamic Disorder, Band Gap Widening, and Persistent Near-IR Photoluminescence up to At Least 523 K in $ASnI_3$ Perovskites ($A = Cs^+$, $CH_3NH_3^+$ and $NH_2-CH=NH_2^+$). *J. Phys. Chem. C* **122**, 26353–26361 (2018).
32. Mukhuti, K., Sinha, S., Sinha, S. & Bansal, B. Dissipation-induced symmetry breaking: Emphanitic transitions in lead- and tin-containing chalcogenides and halide perovskites. *Appl. Phys. Lett.* **118**, 162111 (2021).
33. Zhao, X.-G., Wang, Z., Malyi, O. I. & Zunger, A. Effect of static local distortions vs. dynamic motions on the stability and band gaps of cubic oxide and halide perovskites. *Materials Today* **49**, 107–122 (2021).
34. T. Weller, M., J. Weber, O., F. Henry, P., Pumpo, A. M. D. & C. Hansen, T. Complete structure and cation orientation in the perovskite photovoltaic methylammonium lead iodide between 100 and 352 K. *Chemical Communications* **51**, 4180–4183 (2015).

35. Whitfield, P. S. *et al.* Structures, Phase Transitions and Tricritical Behavior of the Hybrid Perovskite Methyl Ammonium Lead Iodide. *Sci Rep* **6**, 35685 (2016).
36. Xi, J., Zheng, L., Wang, S., Yang, J. & Zhang, W. Temperature-dependent structural fluctuation and its effect on the electronic structure and charge transport in hybrid perovskite CH₃NH₃PbI₃. *Journal of Computational Chemistry* **42**, 2213–2220 (2021).
37. Manser, J. S. & Kamat, P. V. Band filling with free charge carriers in organometal halide perovskites. *Nature Photonics* **8**, 737–743 (2014).
38. Burstein, E. Anomalous Optical Absorption Limit in InSb. *Phys. Rev.* **93**, 632–633 (1954).
39. Moss, T. S. The Interpretation of the Properties of Indium Antimonide. *Proc. Phys. Soc. B* **67**, 775 (1954).
40. Capizzi, M. *et al.* Electron-hole plasma in direct-gap Ga_{1-x}Al_xAs and k-selection rule. *Phys. Rev. B* **29**, 2028–2035 (1984).
41. Kalt, H. & Rinker, M. Band-gap renormalization in semiconductors with multiple inequivalent valleys. *Phys. Rev. B* **45**, 1139–1154 (1992).
42. Lin, R. *et al.* Monolithic all-perovskite tandem solar cells with 24.8% efficiency exploiting comproportionation to suppress Sn(II) oxidation in precursor ink. *Nat Energy* **4**, 864–873 (2019).
43. Francisco-López, A. *et al.* Phase Diagram of Methylammonium/Formamidinium Lead Iodide Perovskite Solid Solutions from Temperature-Dependent Photoluminescence and Raman Spectroscopies. *J. Phys. Chem. C* **124**, 3448–3458 (2020).

44. Weber, O. J., Charles, B. & Weller, M. T. Phase behaviour and composition in the formamidinium–methylammonium hybrid lead iodide perovskite solid solution. *J. Mater. Chem. A* **4**, 15375–15382 (2016).
45. Simenas, M. *et al.* Suppression of phase transitions and glass phase signatures in mixed cation halide perovskites. *Nat Commun* **11**, 5103 (2020).
46. Pierron, E. D., Parker, D. L. & McNeely, J. B. Coefficient of Expansion of GaAs, GaP, and Ga(As, P) Compounds from -62° to 200°C . *Journal of Applied Physics* **38**, 4669–4671 (1967).
47. Miyata, A. *et al.* Direct measurement of the exciton binding energy and effective masses for charge carriers in organic–inorganic tri-halide perovskites. *Nature Physics* **11**, 582–587 (2015).
48. Saba, M. *et al.* Correlated electron–hole plasma in organometal perovskites. *Nat Commun* **5**, 5049 (2014).
49. Sestu, N. *et al.* Absorption F-Sum Rule for the Exciton Binding Energy in Methylammonium Lead Halide Perovskites. *J. Phys. Chem. Lett.* **6**, 4566–4572 (2015).
50. Herz, L. M. Charge-Carrier Dynamics in Organic-Inorganic Metal Halide Perovskites. *Annu. Rev. Phys. Chem.* **67**, 65–89 (2016).
51. Davies, C. L. *et al.* Bimolecular recombination in methylammonium lead triiodide perovskite is an inverse absorption process. *Nat Commun* **9**, 293 (2018).
52. Guo, Y. *et al.* Dynamic emission Stokes shift and liquid-like dielectric solvation of band edge carriers in lead-halide perovskites. *Nature Communications* **10**, 1175 (2019).
53. Parrott, E. S. *et al.* Effect of Structural Phase Transition on Charge-Carrier Lifetimes and Defects in $\text{CH}_3\text{NH}_3\text{SnI}_3$ Perovskite. *J. Phys. Chem. Lett.* **7**, 1321–1326 (2016).

54. Rubino, A. *et al.* Disentangling Electron–Phonon Coupling and Thermal Expansion Effects in the Band Gap Renormalization of Perovskite Nanocrystals. *J. Phys. Chem. Lett.* **12**, 569–575 (2021).
55. Carpenella, V. *et al.* High-Pressure Behavior of δ -Phase of Formamidinium Lead Iodide by Optical Spectroscopies. *J. Phys. Chem. C* **127**, 2440–2447 (2023).
56. Liu, G. *et al.* Pressure-Induced Bandgap Optimization in Lead-Based Perovskites with Prolonged Carrier Lifetime and Ambient Retainability. *Advanced Functional Materials* **27**, 1604208 (2017).
57. Lee, Y., Mitzi, D. B., Barnes, P. W. & Vogt, T. Pressure-induced phase transitions and templating effect in three-dimensional organic-inorganic hybrid perovskites. *Phys. Rev. B* **68**, 020103 (2003).
58. Ning, J. *et al.* Temperature-dependence of the band gap in the all-inorganic perovskite CsPbI₃ from room to high temperatures. *Phys. Chem. Chem. Phys.* **24**, 16003–16010 (2022).
59. Patrick, C. E., Jacobsen, K. W. & Thygesen, K. S. Anharmonic stabilization and band gap renormalization in the perovskite CsSnI₃. *Phys. Rev. B* **92**, 201205 (2015).
60. Carignano, M. A., Aravindh, S. A., Roqan, I. S., Even, J. & Katan, C. Critical Fluctuations and Anharmonicity in Lead Iodide Perovskites from Molecular Dynamics Supercell Simulations. *J. Phys. Chem. C* **121**, 20729–20738 (2017).
61. Price, M. B. *et al.* Hot-carrier cooling and photoinduced refractive index changes in organic–inorganic lead halide perovskites. *Nat Commun* **6**, 8420 (2015).
62. Yang, Y. *et al.* Observation of a hot-phonon bottleneck in lead-iodide perovskites. *Nature Photon* **10**, 53–59 (2016).

63. Mosconi, E., Umari, P. & Angelis, F. D. Electronic and optical properties of mixed Sn–Pb organohalide perovskites: a first principles investigation. *J. Mater. Chem. A* **3**, 9208–9215 (2015).
64. Hamberg, I., Granqvist, C. G., Berggren, K.-F., Sernelius, B. E. & Engström, L. Band-gap widening in heavily Sn-doped In_2O_3 . *Phys. Rev. B* **30**, 3240–3249 (1984).
65. Brinkman, W. F. & Rice, T. M. Electron-Hole Liquids in Semiconductors. *Phys. Rev. B* **7**, 1508–1523 (1973).
66. Feneberg, M. *et al.* Band gap renormalization and Burstein-Moss effect in silicon- and germanium-doped wurtzite GaN up to 10^{20} cm^{-3} . *Phys. Rev. B* **90**, 075203 (2014).
67. Muñoz, M. *et al.* Burstein-Moss shift of n-doped $\text{In}_{0.53}\text{Ga}_{0.47}\text{As}/\text{InP}$. *Phys. Rev. B* **63**, 233302 (2001).
68. Zhang, H. *et al.* Spin Coherence and Spin Relaxation in Hybrid Organic–Inorganic Lead and Mixed Lead–Tin Perovskites. *Nano Lett.* (2023) doi:10.1021/acs.nanolett.3c01734.
69. Kresse, G. & Furthmüller, J. Efficient iterative schemes for ab initio total-energy calculations using a plane-wave basis set. *Phys. Rev. B* **54**, 11169–11186 (1996).
70. Perdew, J. P., Burke, K. & Ernzerhof, M. Generalized Gradient Approximation Made Simple. *Phys. Rev. Lett.* **77**, 3865–3868 (1996).
71. Grimme, S., Antony, J., Ehrlich, S. & Krieg, H. A consistent and accurate ab initio parametrization of density functional dispersion correction (DFT-D) for the 94 elements H–Pu. *J. Chem. Phys.* **132**, 154104 (2010).
72. Becke, A. D. & Johnson, E. R. A simple effective potential for exchange. *J. Chem. Phys.* **124**, 221101 (2006).